

Systematic construction of scarred many-body dynamics in 1D lattice models

Kieran Bull,¹ Ivar Martin,² and Z. Papić¹

¹*School of Physics and Astronomy, University of Leeds, Leeds LS2 9JT, United Kingdom*

²*Materials Science Division, Argonne National Laboratory, Argonne, Illinois 60439, USA*

We introduce a family of non-integrable 1D lattice models that feature robust periodic revivals under a global quench from certain initial product states, thus generalizing the phenomenon of many-body scarring recently observed in Rydberg atom quantum simulators. Our construction is based on a systematic embedding of the single-site unitary dynamics into a kinetically-constrained many-body system. We numerically demonstrate that this construction yields optimal models with the highest amplitude of the wave-function revivals, and it captures all local 1D lattice models that support scars for the fixed choice of the kinetic constraint. We show that general scarring models have a simple interpretation in terms of quantum clock operators, which allows to decompose their dynamics into a period of nearly free clock precession and an interacting bottleneck, shedding light on their anomalously slow thermalization when quenched from special initial states.

Introduction.—The understanding of ergodicity and thermalization in isolated quantum systems is an open problem in many-body physics, with important implications for a variety of experimental systems [1–5]. On the one hand, this problem has inspired important theoretical developments such as the *Eigenstate Thermalization Hypothesis* (ETH) [6–8], which establishes a link between ergodicity and the properties of the system’s eigenstates. On the other hand, strong violation of ergodicity can result in rich new physics, such as in integrable systems [9], Anderson insulators [10], and many-body localized phases [11–13]. In all these cases, the presence of an extensive number of conservation laws prevents the system, initialized in a random state, from fully exploring all allowed configurations in the Hilbert space, causing a strong ergodicity breaking.

A recent experiment on an interacting quantum simulator [14] has reported a surprising observation of quantum dynamics that is suggestive of *weak* ergodicity breaking. Utilizing large 1D chains of Rydberg atoms [14–16], the experiment showed that quenching the system from a Néel initial state lead to persistent revivals of local observables, while other initial states exhibited fast equilibration without any revivals. The stark sensitivity of the system’s dynamics to the initial states, which were all effectively drawn from an “infinite temperature” ensemble, appeared at odds with “strong” ETH [17–19].

In Ref. 20 and 21 the non-ergodic dynamics of a Rydberg atom chain was interpreted as a many-body generalization of the classic phenomenon of *quantum scar* [22]. For a quantum particle in a stadium billiard, scars represent an anomalous concentration of the particle’s trajectory around (unstable) periodic orbits in the corresponding classical system ($\hbar \rightarrow 0$), which has an impact on optical and transport properties of such systems [23–25]. By contrast, in the strongly interacting Rydberg atom chain initialized in the Néel state, quantum dynamics remains concentrated around a small subset of states in the many-body Hilbert space. This effectively gives rise to a “semiclassical” dynamics from the particular initial

state [21], explaining the revivals observed in experiment. Recent works [26, 27] have furthermore shown that revivals can be significantly enhanced by applying certain perturbations to the system. Nevertheless, a general understanding of the necessary conditions that allow scars to occur in a many-body quantum system is still lacking.

The observation of periodic dynamics was linked to the existence of atypical eigenstates at evenly spaced energies throughout the spectrum of the many-body system [20, 28, 29]. Similar phenomenology was previously found in the non-integrable AKLT model [30, 31], where highly-excited eigenstates that feature low entanglement have been analytically constructed. A few of such exact eigenstates are now also available for the Rydberg atom chain model [32]. In a related development, it was proposed that atypical eigenstates of one Hamiltonian can be “embedded” into the spectrum of another, ETH-violating, Hamiltonian [33]. However, even though the collection of models that feature atypical eigenstates is rapidly expanding [34–37], including recent examples of topological phases [38] and fractons [39], their relation to periodic dynamics remains largely unclear.

In this paper we systematically construct interacting lattice models that exhibit periodic quantum revivals. Each lattice site has the Hilbert space containing N_c states (“colors”) and a time-independent Hamiltonian that yields periodic unitary dynamics, $\mathcal{U}(t + T) = \mathcal{U}(t)$. The interacting models are obtained by coupling these building blocks under a kinetic constraint. We show that such a construction generates a family of models that display periodic revivals when quenched from a particular product state. In all the cases, the existence of atypical scarred eigenstates underpins the revivals. Intriguingly, the dynamics in these models can be decomposed into periods of nearly free precession, in which the local degrees of freedom coherently cycle through the available states on a single site, followed by an interacting segment of dynamical evolution, reminiscent of a kicked quantum top [40]. We numerically demonstrate that our construction yields optimal models (i.e., with the highest ampli-

tude of the wave function revivals) for an arbitrary number of colors. Moreover, we show that our construction includes known models, such as chiral clock models [41], which are shown to support scars, and also gives a way of enhancing the revivals in spin- s generalisations of the Rydberg chain [21].

PXP model.—We start by briefly reviewing the model of a strongly-interacting 1D Rydberg atom chain [42–45]. The system can be modelled as coupled two level systems (with states $|0\rangle$, $|1\rangle$) described by an effective “PXP” Hamiltonian

$$H = \sum_j P_{j-1}^0 X_j P_{j+1}^0, \quad P_j^0 \equiv |0_j\rangle\langle 0_j|, \quad (1)$$

where $X_j = |0_j\rangle\langle 1_j| + |1_j\rangle\langle 0_j|$ denotes the Pauli matrix. The model in Eq. (1) describes a kinetically constrained paramagnet [46]: each atom can flip only if both its neighbours are in $|0\rangle$ state.

The Hamiltonian in Eq. (1) is interacting and non-integrable [20], yet it exhibits unconventional thermalization. For example, the model has atypical (ETH-violating) eigenstates with low entanglement at high energy densities [28]. Moreover, when the system is quenched from the Néel initial state, $|\psi_0\rangle = |0101\dots\rangle$, local observables such as domain wall density [14] and even the many-body wave function fidelity, $F(t) = |\langle\psi_0|\psi(t)\rangle|^2$, all revive with the same frequency [20, 37, 47]. At the same time, quenches from other initial states, such as $|0000\dots\rangle$, do not lead to observable revivals [14]. The revival frequency from the Néel state was found to be set by the energy separation between atypical eigenstates with lowest entanglement entropy, as the same eigenstates also happen to maximize the overlap with the Néel state [20]. Thus, the quench dynamics from the Néel state is largely restricted to a subset of many-body eigenstates, and can be viewed as a precession of a large spin, tracing a periodic orbit that can be accurately captured by time-dependent variational principle (TDVP) on a manifold of matrix product states with bond dimension 2 [21].

Construction of scarred models.— Consider now a system with a local basis $|0\rangle$, $|1\rangle$, ..., $|N_c - 1\rangle$, and an arbitrary time independent Hamiltonian h whose unitary dynamics is periodic, such that $\mathcal{U}^T \equiv \exp(-ihT) = \mathbb{I}$ for arbitrary T (not necessarily integer). The eigenvalues of \mathcal{U} are then $\lambda_n = \exp(i2\pi k_n/T)$, with the corresponding eigenvectors $|\psi_n\rangle$, where k_n are arbitrary integers. In the examples below, we primarily focus on cases where h is off-diagonal in the color basis, which is satisfied when $\{k_n\}$ are chosen symmetric around zero. Then, we can obtain candidate Hamiltonians h by choosing particular $\{\lambda_n\}$ which guarantee a periodic \mathcal{U} and taking its logarithm:

$$h = i \sum_{n=0}^{N_c-1} \frac{2\pi i}{T} k_n |\psi_n\rangle\langle\psi_n|. \quad (2)$$

To define a many-body lattice Hamiltonian, we take a tensor product of h and impose a kinetic constraint that h only acts on sites whose neighbours are in some unlocking state $|\phi\rangle$:

$$H = \sum_j P_{j-1} h_j P_{j+1}, \quad P_j \equiv |\phi_j\rangle\langle\phi_j|. \quad (3)$$

An important special case of this construction is when \mathcal{U} is interpreted as the shift operator of a quantum clock [41, 48], as we explain next.

Scars in clock models.—The scarred clock models are defined by choosing $T = N_c$, which gives

$$\mathcal{U} = e^{-iC} = \sum_{j=0}^{N_c-1} |j+1\rangle\langle j|. \quad (4)$$

In this case, $\lambda_n = \exp(2\pi i k_n/N_c)$ and $|\psi_n\rangle = \sum_{j=0}^{N_c-1} (1/\lambda_n^j) |j\rangle$. For odd N_c , k_n takes the values $-\frac{N_c-1}{2}, \dots, 0, \dots, \frac{N_c-1}{2}$. For N_c -even, we need to double the period, $T = 2N_c$, in order to make h off-diagonal. This allows to choose $k = -\frac{N_c-1}{2}, \dots, -\frac{1}{2}, \frac{1}{2}, \dots, \frac{N_c-1}{2}$, and Eq. (S1) continues to be valid for N_c -even after performing a gauge transformation, $|j\rangle \rightarrow e^{i\pi j/N_c} |j\rangle$.

The inspiration behind \mathcal{U} in Eq. (S1) is that local dynamics is a cyclic rotation around the basis of N_c “clock” states $|j\rangle$, Fig. 1(a). The many-clock “PCP” Hamiltonian from Eq. (3) then becomes

$$H_{\text{clock}} = \sum_j P_{j-1}^0 C_j P_{j+1}^0, \quad (5)$$

with C represents h in Eq. (2). Because the local dynamics is cyclic, without loss of generality we can choose the projector onto any of the clock basis states, e.g., $P^0 = |0\rangle\langle 0|$. The PCP model has a simple interpretation in the clock basis, Fig 1(a): each site precesses around the clock of basis states if both its neighbours are in $|0\rangle$ state, otherwise the site remains frozen.

We have studied the PCP model in Eq. (5) using exact diagonalization, assuming periodic boundary conditions. For any $N_c \leq 8$ accessible to us numerically, we find long-lived oscillatory dynamics when the system is quenched from any Néel-like state, $|0101\dots\rangle$, $|0202\dots\rangle$, etc. Fig. 1(b) summarizes the result for $N_c = 4$. The dynamics proceeds in two steps. First, each unfrozen clock nearly freely cycles through its states, $|1\rangle \rightarrow |2\rangle \rightarrow \dots |N_c - 1\rangle$. After this coherent process is complete, the many-clock state shifts, $|N_c - 1, 0, N_c - 1, 0\dots\rangle \rightarrow |0101\dots\rangle$. In this second step, interactions kick in and some fidelity is lost to thermalization. This cycle of free precession followed by a short interacting segment is reminiscent of a kicked quantum top. We now see that PXP model (which is equivalent to $N_c = 2$ clock) is special in that it lacks a free-precession segment in the dynamics. On the other hand, similar to the PXP case, in scarred clock models

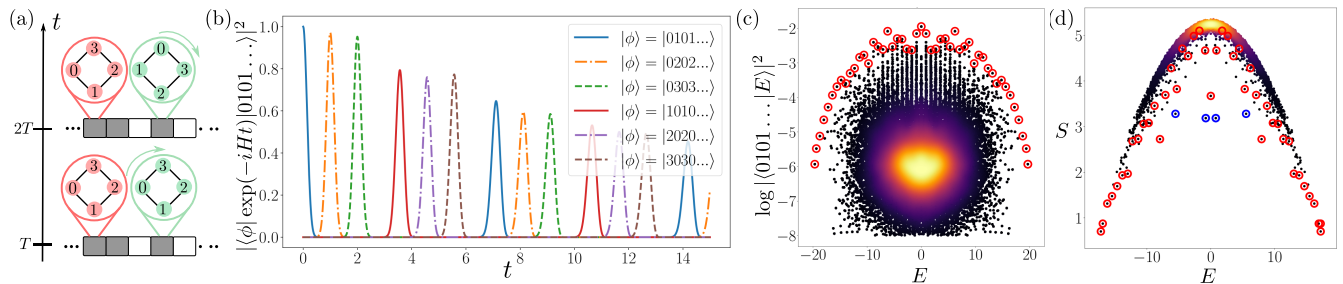


Figure 1. (a) A schematic of scarred clock models. A clock (green) can precess because both of its neighbours are in the unlocking state $|0\rangle$ (white), unlike the frozen clock (red). (b) Dynamics of fidelity, $|\langle\phi|\exp(-itH)|0101\dots\rangle|^2$, for $N_c = 4$ -color clock model in Eq. (5). Different curves correspond to several choices of $|\phi\rangle$: the initial state $|1010\dots\rangle$, the product state of shifted clocks $|n0n0\dots\rangle$ ($n = 2, 3, \dots, N_c - 1$), or the overall translation of the initial state, $|0101\dots\rangle$. (c) Overlap of all eigenstates of $N_c = 4$ -color clock model with the Néel state $|0101\dots\rangle$. Each dot represents a (logarithm) of the overlap for an eigenstate $|E\rangle$ with energy E shown on the x -axis. Color scale indicates the density of data points in the bulk of the spectrum. Scarred states are marked by red circles. (d) Entanglement entropy S of all eigenstates of $N_c = 4$ -color clock model, plotted as a function of their energy E . Entropy is evaluated for the symmetric bipartition of the system. Red circles indicate the matching scarred states from (c), while a few additional scar states, associated with the “ Z_4 ” state $|20002000\dots\rangle$, are marked by blue circles. Plots (b), (c) are for system size $N = 16$, while (d) is for $N = 14$. In all cases, we resolve translation and inversion symmetry, and plot both $[k = 0, P = +]$ and $[k = \pi, P = -]$ sectors.

coherence also remains protected to a large degree during the interacting part of the process, allowing the wave function to keep returning to the initial state at later times.

In order to visualize the dynamics, in Fig. 1(b) we plot the fidelity $|\langle\phi|\exp(-itH)|0101\dots\rangle|^2$ w.r.t. several product states $|\phi\rangle$ corresponding to either the initial state, the internal shift of each clock, or to the overall translation of the initial state. The duration of individual clock ticks (e.g., $|1010\dots\rangle \rightarrow |2020\dots\rangle$) matches that of the *unconstrained* clock model. Following the convention that C is rescaled such that nearest neighbour hoppings have magnitude one, the frequency of the putative free precession is found to be ≈ 0.9016 (in units $\hbar = 1$) while the frequency of the single site precession (in the absence of a constraint) is ≈ 0.9003 . We note that time evolution of local observables is consistent with the presented picture of the underlying dynamics [49].

In Fig. 1(c) we show the overlap of all eigenstates with the Néel state $|0101\dots\rangle$, while Fig. 1(d) shows the bipartite entanglement entropy $S = -\text{tr}\rho_A \ln \rho_A$, where ρ_A is the reduced density matrix of one half of the chain. The scar states are easily identifiable as a band of special eigenstates (circled in red) that extend throughout the spectrum. Total number of special states is $(N_c - 1)N + 1$. Similar to the PXP model, the special eigenstates are distinguished by their high overlap with the Néel state, or alternatively as ones with atypically low entanglement. We note that some of the eigenstates with smallest entanglement belong to a different band of scarred states associated with the “ Z_4 ” state $|20002000\dots\rangle$ (blue circles in Fig. 1(d)). Apart from these special states, we also observe tower structures in the spectrum, which reflect the clustering of neighboring eigenstates around the energies

of the scarred eigenstates. Deep in the bulk of the spectrum, the density of states [indicated by color scheme in Fig. 1(c)] appears to be uniform, as expected from the ETH. Indeed, at $N = 14$ we find a mean level spacing ratio [50] of $\langle r \rangle = 0.5218$, consistent with Wigner-Dyson statistics and the ETH. We have confirmed that the frequency of the revival to the initial state matches the energy separation between special eigenstates in Fig. 1(c).

Relation to spin- s and chiral clock models.—In Ref. [21] the TDVP approach was generalized to spin- s PXP models with the kinetic constraint P^0 , and the existence of periodic revivals was numerically demonstrated in $s = 1, 2$ cases. Our PCP model in Eq. (5) can be deformed into a spin- s PXP model by taking $k = -s, \dots, s$ and performing a basis rotation, resulting in $H_{\text{clock}} = \sum_j P'_{j-1} X_j P'_{j+1}$, where P' is a deformation of the projector P^0 in Eq. (5) [49]. We have numerically found that the number of scarred states remains the same for PXP models expressed in terms of either the spin P^0 or P' ; however, the amplitude of the revivals is always higher when using P' instead of spin P^0 for N_c -odd [49]. Thus, our construction shows how to improve the revivals in the standard PXP models. In addition, mapping to a clock representation allows to clearly delineate nearly-free precession from the interacting part of the dynamics, which is not transparent in the spin representation.

Furthermore, our construction admits models for which C is not related to spin matrices via a change of basis. One family of models for even N_c is obtained by choosing $k = -\frac{N_c}{2}, \dots, -1, 1, \dots, \frac{N_c}{2}$, with the same projector P^0 as above. For $N_c = 4$, the resulting C is equivalent to a 4-color Chiral Clock Model (CCM) at the fixed point in the disordered phase [41, 49, 51]. This model features two types of oscillatory dynamics [49].

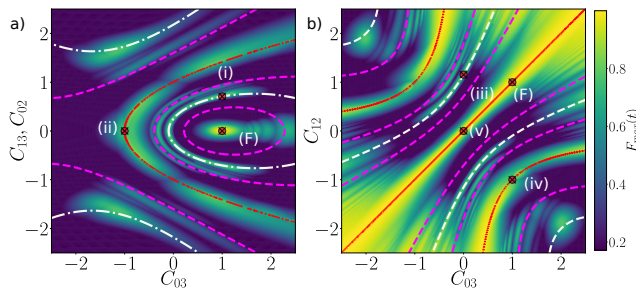


Figure 2. The phase diagram of scarred models with local Hilbert space dimension $N_c = 4$ and projector P^0 . Shown in (a), (b) are two slices of the phase diagram obtained by varying the matrix elements of C , indicated on the axes. Color scale represents the maximum of the first fidelity revival for quenches from any of the states $|0101\dots\rangle$, $|0202\dots\rangle$, $|0303\dots\rangle$. Results are for $N_c = 4$ and system size $N = 10$. Labels on the diagrams refer to special limiting cases defined in the text. Scarred models can be accurately predicted based on the commensurability of the eigenvalue spectrum of C . For example, eigenvalues of C can be evenly spaced, as in clock model in Eq. (5) (white line), or they can be degenerate as in CCM (red dots). There are also more fragile models realized when the spacings between C eigenvalues are in simple ratios like 1:2 (pink line).

When a single site is initialized in $|1\rangle$, the dynamics of C primarily leads to the transition $|1\rangle \rightarrow |3\rangle$, with much smaller probability ($\frac{1}{4}$) for other transitions, such as $|1\rangle \rightarrow |2\rangle$. Similarly, when initialized in $|2\rangle$, the dominant process is $|2\rangle \rightarrow |0\rangle$. Thus, in a many-body system with the constraint P^0 , we expect different behavior for initial states $|0101\dots\rangle$, $|0303\dots\rangle$ compared to $|0202\dots\rangle$, $|0404\dots\rangle$. In the former case, dynamics is essentially that of a free paramagnet oscillating between $|0101\dots\rangle \rightarrow |0303\dots\rangle$. In the latter case, dynamics follows the pattern $|0202\dots\rangle \rightarrow |0000\dots\rangle$, after which an exchange of sublattices is permitted, $|0000\dots\rangle \rightarrow |2020\dots\rangle$, and the scarring phenomenology is similar to spin- $\frac{1}{2}$ PXP model. We note, however, that for larger N_c , our construction yields C 's that are no longer equivalent to CCMs, due to longer range couplings between the basis states. Nevertheless, the dynamics for general $N_c \leq 6$ that we have investigated in detail can still be approximately described as either the nearly-free paramagnet precession or the PXP-like periodic oscillation.

General phase diagram of scarred models.—We now perform an exhaustive search for general scarred models with the fixed kinetic constraint P^0 . By varying all off-diagonal elements of C , we scan all models of the form Eq. (5), with C containing no diagonal entries. We map out the phase diagram of these models based on the quality of scars, i.e., the first revival maximum of the fidelity from the Néel-like states. We keep the matrix elements of C purely imaginary, as introducing real couplings was typically found to weaken the revivals.

As an example, we map the phase diagram of the

$N_c = 4$ case. This requires varying 5 matrix elements in C , so we restrict to taking slices where only two parameters are simultaneously varied. We consider two cases, (a) vary the next-nearest-neighbor hoppings $C_{02} = C_{13} = \alpha i$, while also varying $C_{03} = -\beta i$, or (b) switch off next-nearest-neighbor hoppings, while varying $C_{12} = -\alpha i$ and $C_{03} = -\beta i$. The corresponding phase diagrams are shown in Fig. 2. On these diagrams there are several limiting cases at special values of (β, α) . For variation (a), we have: (i) $(1, 1/\sqrt{2})$ is $N_c = 4$ clock; (ii) $(-1, 0)$ is $N_c = 4$ CCM model. For variation (b): (iii) $(0, 2/\sqrt{3})$ is spin- $\frac{3}{2}$ PXP; (iv) $(1, -1)$ is also $N_c = 4$ CCM; (v) at $(0, 0)$, we have $C = i \sum_{j=0,2} |j\rangle\langle j+1|$ -h.c., which (with P^0) can be viewed as the sum of a spin- $\frac{1}{2}$ PXP and a free $s = \frac{1}{2}$ paramagnet. Points marked F correspond to decoupled free paramagnets.

The maximum fidelity at first revival for N_c -even is generally comparable between clock and spin- s PXP models. For example, for $N_c = 4$ in Fig. 2, $F_{max} \approx 0.7613$ (clock) and $F_{max} \approx 0.7825$ for spin- $\frac{3}{2}$ PXP. For $N_c = 6$ and $N = 8$, we obtain $F_{max} \approx 0.813$ (spin) and $F_{max} \approx 0.802$ (clock), while for $N_c = 8$, $N = 8$ we find $F_{max} \approx 0.7927$ (spin) and $F_{max} \approx 0.8059$ (clock). On the other hand, for N_c -odd, we find a considerable improvement in the fidelity of a clock compared to the spin- s PXP model. For example, for $N_c = 3$, the maximum fidelity of the clock model is $F_{max} \approx 0.7237$ versus $F_{max} \approx 0.6534$ for spin-1; for $N_c = 5$, $N = 10$, the improvement is even bigger, $F_{max} \approx 0.5626$ vs. $F_{max} \approx 0.7656$ (clock) [49]. Thus, our construction for odd N_c gives a way to improve the revivals of spin- s PXP models.

Since the phase diagram in Fig. 2 is evidently quite rich, we look for a simple guiding principle that predicts the parameters of the most robust scarring models. Such a criterion is provided by the commensurability of the eigenvalue spectrum of C , which we illustrate by lines and dots in Fig. 2. White line marks the models for which C has equidistant energy levels, i.e., its eigenvalues are $E_n = k\epsilon$, $k \in \mathbb{Z}$. Our $N_c = 4$ clock model lies on one of these lines, as shown in Fig. 2(a). We can consider further commensurability conditions where the energy spacings of C are in simple ratios, e.g., 1:2 (pink lines). Finally, red points mark the areas where C contains one pair of degenerate eigenvalues (which in our case, trivially, have commensurate spacing). One of these points hosts the $N_c = 4$ CCM at its fixed point in the disordered phase. Another one, along the diagonal in Fig. 2(b), hosts a combination of the free paramagnet and spin- $\frac{1}{2}$ PXP model. We emphasize, however, that our simple criterion based on the non-interacting spectrum of C only serves as a rough indicator of scarring models. The precise parameter values where such models are realized are determined by the non-trivial compatibility between this condition and the kinetic constraint, i.e., the projectors P^0 .

Conclusion—We have presented a systematic construction of non-integrable models that feature periodic re-

vivals in the quench dynamics from the Néel-type initial states. Our construction yields quantum clock models with arbitrary numbers of colors, whose couplings are close to their optimal values, resulting in the highest revival fidelity. We numerically found that all known models exhibiting strong revivals (for the given choice of the kinetic constraint P^0) can be obtained from our general construction, including in particular the higher-spin PXP models and CCMs. There are two types of behaviour when these models are kinetically constrained. They can decouple, leaving the 0 sublattice of a Néel state frozen as a direct consequence of the kinetic constraint, resulting in near perfect revivals. Alternatively, if the single site precession and constraint permit an exchange of sublattices, we instead see alternative behaviour, where a period of free precession is followed by a shedding of fidelity as sublattices are exchanged.

Acknowledgements.—K.B. and Z.P. acknowledge support by EPSRC grants EP/P009409/1 and EP/R020612/1. Statement of compliance with EPSRC policy framework on research data: This publication is theoretical work that does not require supporting research data. This research was supported in part by the National Science Foundation under Grant No. NSF PHY-1748958. Work at Argonne National Laboratory was supported by the Department of Energy, Office of Science, Materials Science and Engineering Division.

-
- [1] Toshiya Kinoshita, Trevor Wenger, and David S. Weiss, “A quantum Newton’s cradle,” *Nature* **440**, 900–903 (2006).
- [2] Michael Schreiber, Sean S. Hodgman, Pranjali Bordia, Henrik P. Lüschen, Mark H. Fischer, Ronen Vosk, Ehud Altman, Ulrich Schneider, and Immanuel Bloch, “Observation of many-body localization of interacting fermions in a quasirandom optical lattice,” *Science* **349**, 842–845 (2015).
- [3] J. Smith, A. Lee, P. Richerme, B. Neyenhuis, P. W. Hess, P. Hauke, M. Heyl, D. A. Huse, and C. Monroe, “Many-body localization in a quantum simulator with programmable random disorder,” *Nat Phys* **12**, 907–911 (2016).
- [4] G. Kucsko, S. Choi, J. Choi, P. C. Maurer, H. Sumiya, S. Onoda, J. Isoya, F. Jelezko, E. Demler, N. Y. Yao, and M. D. Lukin, “Critical thermalization of a disordered dipolar spin system in diamond,” ArXiv e-prints (2016), [arXiv:1609.08216](https://arxiv.org/abs/1609.08216).
- [5] Adam M. Kaufman, M. Eric Tai, Alexander Lukin, Matthew Rispoli, Robert Schittko, Philipp M. Preiss, and Markus Greiner, “Quantum thermalization through entanglement in an isolated many-body system,” *Science* **353**, 794–800 (2016).
- [6] J. M. Deutsch, “Quantum statistical mechanics in a closed system,” *Phys. Rev. A* **43**, 2046–2049 (1991).
- [7] Mark Srednicki, “Chaos and quantum thermalization,” *Phys. Rev. E* **50**, 888–901 (1994).
- [8] Marcos Rigol, Vanja Dunjko, and Maxim Olshanii, “Thermalization and its mechanism for generic isolated quantum systems,” *Nature* **452**, 854–858 (2008).
- [9] B. Sutherland, *Beautiful Models: 70 Years of Exactly Solved Quantum Many-body Problems* (World Scientific, 2004).
- [10] P. W. Anderson, “Absence of diffusion in certain random lattices,” *Phys. Rev.* **109**, 1492–1505 (1958).
- [11] D.M. Basko, I.L. Aleiner, and B.L. Altshuler, “Metal–insulator transition in a weakly interacting many-electron system with localized single-particle states,” *Annals of Physics* **321**, 1126 – 1205 (2006).
- [12] Maksym Serbyn, Z. Papić, and Dmitry A. Abanin, “Local conservation laws and the structure of the many-body localized states,” *Phys. Rev. Lett.* **111**, 127201 (2013).
- [13] David A. Huse, Rahul Nandkishore, and Vadim Oganesyan, “Phenomenology of fully many-body-localized systems,” *Phys. Rev. B* **90**, 174202 (2014).
- [14] Hannes Bernien, Sylvain Schwartz, Alexander Keesling, Harry Levine, Ahmed Omran, Hannes Pichler, Soonwon Choi, Alexander S. Zibrov, Manuel Endres, Markus Greiner, Vladan Vuletic, and Mikhail D. Lukin, “Probing many-body dynamics on a 51-atom quantum simulator,” *Nature* **551**, 579 (2017).
- [15] Peter Schauß, Marc Cheneau, Manuel Endres, Takeshi Fukuhara, Sebastian Hild, Ahmed Omran, Thomas Pohl, Christian Gross, Stefan Kuhr, and Immanuel Bloch, “Observation of spatially ordered structures in a two-dimensional Rydberg gas,” *Nature* **491**, 87 EP – (2012).
- [16] Henning Labuhn, Daniel Barredo, Sylvain Ravets, Sylvain de Léséleuc, Tommaso Macrì, Thierry Lahaye, and Antoine Browaeys, “Tunable two-dimensional arrays of single Rydberg atoms for realizing quantum Ising models,” *Nature* **534**, 667 (2016).
- [17] Luca D’Alessio, Yariv Kafri, Anatoli Polkovnikov, and Marcos Rigol, “From quantum chaos and eigenstate thermalization to statistical mechanics and thermodynamics,” *Advances in Physics* **65**, 239–362 (2016).
- [18] Christian Gogolin and Jens Eisert, “Equilibration, thermalisation, and the emergence of statistical mechanics in closed quantum systems,” *Reports on Progress in Physics* **79**, 056001 (2016).
- [19] Takashi Mori, Tatsuhiko N Ikeda, Eriko Kaminishi, and Masahito Ueda, “Thermalization and prethermalization in isolated quantum systems: a theoretical overview,” *Journal of Physics B: Atomic, Molecular and Optical Physics* **51**, 112001 (2018).
- [20] C. J. Turner, A. A. Michailidis, D. A. Abanin, M. Serbyn, and Z. Papić, “Weak ergodicity breaking from quantum many-body scars,” *Nature Physics* (2018), [10.1038/s41567-018-0137-5](https://doi.org/10.1038/s41567-018-0137-5).
- [21] Wen Wei Ho, Soonwon Choi, Hannes Pichler, and Mikhail D. Lukin, “Periodic orbits, entanglement, and quantum many-body scars in constrained models: Matrix product state approach,” *Phys. Rev. Lett.* **122**, 040603 (2019).
- [22] Eric J. Heller, “Bound-state eigenfunctions of classically chaotic hamiltonian systems: Scars of periodic orbits,” *Phys. Rev. Lett.* **53**, 1515–1518 (1984).
- [23] S. Sridhar, “Experimental observation of scarred eigenfunctions of chaotic microwave cavities,” *Phys. Rev. Lett.* **67**, 785–788 (1991).
- [24] C. M. Marcus, A. J. Rimberg, R. M. Westervelt, P. F. Hopkins, and A. C. Gossard, “Conductance fluctuations and chaotic scattering in ballistic microstructures,” *Phys.*

- Rev. Lett.* **69**, 506–509 (1992).
- [25] P. B. Wilkinson, T. M. Fromhold, L. Eaves, F. W. Sheard, N. Miura, and T. Takamasu, “Observation of scarred wavefunctions in a quantum well with chaotic electron dynamics,” *Nature* **380**, 608 EP – (1996).
- [26] V. Khemani, C. R. Laumann, and A. Chandran, “Signatures of integrability in the dynamics of Rydberg-blockaded chains,” ArXiv e-prints (2018), [arXiv:1807.02108 \[cond-mat.str-el\]](#).
- [27] Soonwon Choi, Christopher J. Turner, Hannes Pichler, Wen Wei Ho, Alexios A. Michailidis, Zlatko Papić, Maksym Serbyn, Mikhail D. Lukin, and Dmitry A. Abanin, “Emergent SU(2) dynamics and perfect quantum many-body scars,” arXiv e-prints , arXiv:1812.05561 (2018), [arXiv:1812.05561 \[quant-ph\]](#).
- [28] C. J. Turner, A. A. Michailidis, D. A. Abanin, M. Serbyn, and Z. Papić, “Quantum scarred eigenstates in a Rydberg atom chain: Entanglement, breakdown of thermalization, and stability to perturbations,” *Phys. Rev. B* **98**, 155134 (2018).
- [29] Thomas Iadecola, Michael Schechter, and Shenglong Xu, “Quantum Many-Body Scars and Space-Time Crystalline Order from Magnon Condensation,” arXiv e-prints , arXiv:1903.10517 (2019), [arXiv:1903.10517 \[cond-mat.str-el\]](#).
- [30] Sanjay Moudgalya, Stephan Rachel, Bogdan A Bernevig, and Nicolas Regnault, “Exact Excited States of Non-Integrable Models,” ArXiv e-prints (2017), [arXiv:1708.05021](#).
- [31] S. Moudgalya, N. Regnault, and B. A. Bernevig, “Entanglement of Exact Excited States of AKLT Models: Exact Results, Many-Body Scars and the Violation of Strong ETH,” ArXiv e-prints (2018), [arXiv:1806.09624](#).
- [32] Cheng-Ju Lin and Olexei I. Motrunich, “Exact Strong-ETH Violating Eigenstates in the Rydberg-blockaded Atom Chain,” arXiv e-prints , arXiv:1810.00888 (2018), [arXiv:1810.00888 \[cond-mat.quant-gas\]](#).
- [33] Naoto Shiraishi and Takashi Mori, “Systematic construction of counterexamples to the eigenstate thermalization hypothesis,” *Phys. Rev. Lett.* **119**, 030601 (2017).
- [34] Andrew J. A. James, Robert M. Konik, and Neil J. Robinson, “Nonthermal states arising from confinement in one and two dimensions,” arXiv e-prints , arXiv:1804.09990 (2018), [arXiv:1804.09990 \[cond-mat.stat-mech\]](#).
- [35] Neil J. Robinson, Andrew J. A. James, and Robert M. Konik, “Signatures of rare states and thermalization in a theory with confinement,” arXiv e-prints , arXiv:1808.10782 (2018), [arXiv:1808.10782 \[cond-mat.str-el\]](#).
- [36] Thomas Iadecola and Marko Znidaric, “Exact localized and ballistic eigenstates in disordered chaotic spin ladders and the Fermi-Hubbard model,” arXiv e-prints , arXiv:1811.07903 (2018), [arXiv:1811.07903 \[cond-mat.str-el\]](#).
- [37] Federica M. Surace, Paolo P. Mazza, Giuliano Giudici, Alessio Lerose, Andrea Gambassi, and Marcello Dalmonte, “Lattice gauge theories and string dynamics in Rydberg atom quantum simulators,” arXiv e-prints , arXiv:1902.09551 (2019), [arXiv:1902.09551 \[cond-mat.quant-gas\]](#).
- [38] Seulgi Ok, Kenny Choo, Christopher Mudry, Claudio Castelnovo, Claudio Chamon, and Titus Neupert, “Topological many-body scar states in dimensions 1, 2, and 3,” arXiv e-prints , arXiv:1901.01260 (2019), [arXiv:1901.01260 \[cond-mat.other\]](#).
- [39] Shriya Pai, Michael Pretko, and Rahul M. Nandkishore, “Robust quantum many-body scars in fraction systems,” arXiv e-prints , arXiv:1903.06173 (2019), [arXiv:1903.06173 \[cond-mat.stat-mech\]](#).
- [40] F. Haake, *Quantum Signatures of Chaos*, Physics and astronomy online library (Springer, 2001).
- [41] Paul Fendley, “Free parafermions,” *Journal of Physics A: Mathematical and Theoretical* **47**, 075001 (2014).
- [42] B Sun and F Robicieux, “Numerical study of two-body correlation in a 1d lattice with perfect blockade,” *New Journal of Physics* **10**, 045032 (2008).
- [43] B. Olmos, R. González-Férez, and I. Lesanovsky, “Collective rydberg excitations of an atomic gas confined in a ring lattice,” *Phys. Rev. A* **79**, 043419 (2009).
- [44] B Olmos, R González-Férez, I Lesanovsky, and L Velázquez, “Universal time evolution of a Rydberg lattice gas with perfect blockade,” *Journal of Physics A: Mathematical and Theoretical* **45**, 325301 (2012).
- [45] Igor Lesanovsky and Hosho Katsura, “Interacting Fibonacci anyons in a Rydberg gas,” *Phys. Rev. A* **86**, 041601 (2012).
- [46] Maike Ostmann, Matteo Marcuzzi, Juan P. Garrahan, and Igor Lesanovsky, “Localization in spin chains with facilitation constraints and disordered interactions,” arXiv e-prints , arXiv:1811.01667 (2018), [arXiv:1811.01667 \[cond-mat.quant-gas\]](#).
- [47] Michael Schechter and Thomas Iadecola, “Many-body spectral reflection symmetry and protected infinite-temperature degeneracy,” *Phys. Rev. B* **98**, 035139 (2018).
- [48] Eric Vernier, Edward O’Brien, and Paul Fendley, “Onsager symmetries in $U(1)$ -invariant clock models,” arXiv e-prints , arXiv:1812.09091 (2018), [arXiv:1812.09091 \[cond-mat.stat-mech\]](#).
- [49] “Supplemental online material.”
- [50] Vadim Oganesyan and David A. Huse, “Localization of interacting fermions at high temperature,” *Phys. Rev. B* **75**, 155111 (2007).
- [51] R.J. Baxter, “A simple solvable Z_N Hamiltonian,” *Physics Letters A* **140**, 155 – 157 (1989).

Supplemental Online Material for “Systematic construction of scarred many-body dynamics in 1D lattice models”

In this supplementary material, we discuss in detail the relation between the clock models introduced in the main text, the spin- s PXP models, and chiral clock models (CCMs). We complement the results for the fidelity dynamics in the main text with a study of dynamics of local observables following the quench. Finally, we show that scarred eigenstates in clock models can be captured using a Krylov-type approximation scheme.

REVIVALS OF LOCAL OBSERVABLES

In the main text we analyzed the dynamics in the clock models from the perspective of fidelity revivals, i.e., the many-body wave function returning to a particular product state after time t . By inspecting different product states, we have concluded that the dynamics proceeds in two steps: (i) precession of every clock between the available basis states; (ii) transition to a product state that is related to the initial state by an overall translation of the system by one lattice site, e.g., $|1010\dots\rangle \rightarrow |0101\dots\rangle$. While the process (i) is nearly free (and hence coherent), remarkably even the process (ii) results in a relatively small loss of fidelity.

Revival of a many-body wave function, of course, is formidable to measure experimentally, and here we demonstrate that the same picture of the dynamics can be inferred from studying revivals in local observables, Q . For example, measuring a color on a given site, $Q \equiv P^n = |n\rangle\langle n|$ will show the same pattern of dynamics, see Fig. S1. Consider the two sublattices, corresponding to even and odd sites. When the system is quenched from the Néel state $|0101\dots\rangle$, even sites initially cycle through the basis set $1 \rightarrow 2 \rightarrow 3\dots$ while odd sites are locked at 0 by the constraint. These sublattices exchange and the process repeats after a full precession $1 \rightarrow 0$ has been completed.

RELATION BETWEEN CLOCK AND SPIN- s PXP MODELS

In the main text we pointed out that spin- s PXP models are included in our construction as a special case. From the definition of \mathcal{U} governing the free precession of our clock models, which we reproduce here,

$$\mathcal{U} = e^{-iC} = \sum_{j=0}^{N_c-1} |j+1\rangle\langle j|. \quad (\text{S1})$$

the eigenvalues are found to be $\lambda_n = \exp(2\pi i k_n / N_c)$, with $k_n \in \{-(N_c-1)/2, \dots, 0, \dots, (N_c-1)/2\}$ for odd N_c , while $k_n \in \{-(N_c-1)/2, \dots, -1/2, 1/2, \dots, (N_c-1)/2\}$ for even N_c . This then implies the eigenvalues of $C \propto i \ln(\mathcal{U})$ are proportional to k_n , which we immediately recognize as angular momenta quantum numbers for spin $2s+1 = N_c$. This tells us that the operators C and X are equivalent by a change of basis.

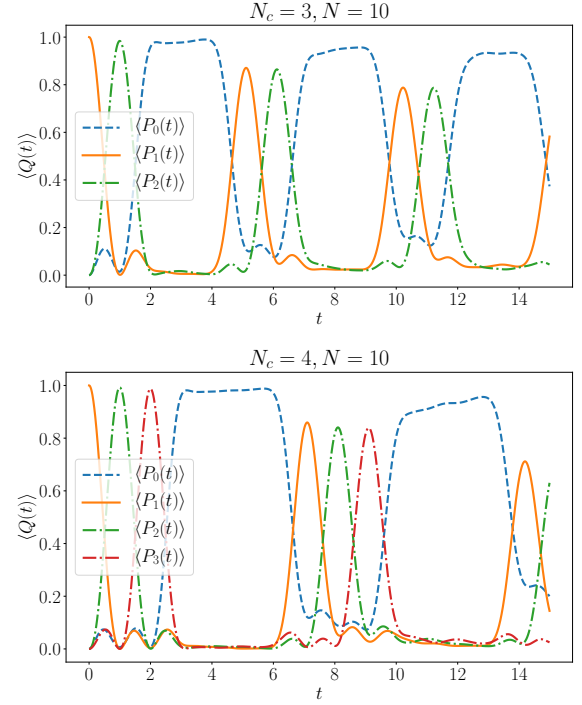


Figure S1. Time evolution of local observables when the PCP model is quenched from the Néel state $|0101\dots\rangle$. Plots show the time evolution of the average color on a given site, $\langle P^n(t) \rangle$, as a function of time. Top plot is for $N_c = 3$ and bottom plot is $N_c = 4$, with system size $N = 10$. A period of free precession can be observed where the sublattice containing 1 cycles through the clock basis, followed by a period of time where the colour on the site is locked to 0 while the other sublattice cycles through the clock basis.

The distinction between the clock and spin models thus lies entirely in the kinetic constraint, i.e., the choice of projector $P = |\phi\rangle\langle\phi|$. For example, at $N_c = 3$, we find:

$$H_{\text{clock}} = \sum_n P_{n-1}^0 C_n P_{n+1}^0, \quad P^0 = \begin{pmatrix} 1 & 0 & 0 \\ 0 & 0 & 0 \\ 0 & 0 & 0 \end{pmatrix} \quad (\text{S2})$$

$$= \sum_n P'_{n-1} X_n P'_{n+1}, \quad P' = \begin{pmatrix} 1/6 & 1/3 & -1/6 \\ 1/3 & 2/3 & -1/3 \\ -1/6 & -1/3 & 1/6 \end{pmatrix} \quad (\text{S3})$$

For $N_c = 3$, it is straightforward to visualize the entire phase diagram with the fixed projector P^0 . There are two couplings to vary, as by a rescaling of C we are free

to fix the value of one of the three couplings. The resulting phase diagram for $N_c = 3$ is shown in Fig. S2 as a function of C_{02} and C_{12} matrix elements. All the

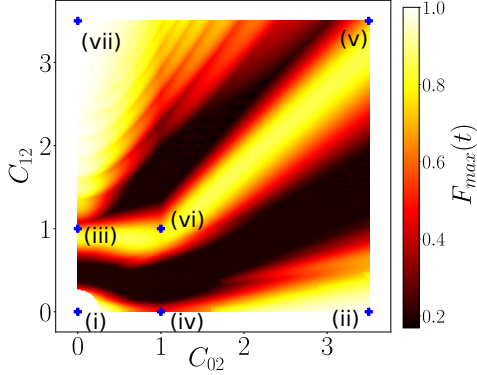


Figure S2. Phase diagram of the $N_c = 3$ models obtained by varying the two matrix elements, C_{02} and C_{12} . Color scale indicates the average maximum of the first fidelity revival quenched from the Néel states $|0101\dots\rangle$ and $|0202\dots\rangle$. All regions associated with strong scarring can be identified with either the spin or clock models.

regions in the diagram that display strong scarring can be interpreted as deformations of one of our previously discussed models. Specifically, in Fig. S2 we identify the representative points as: (i) and (ii) are spin- $\frac{1}{2}$ PXP, (iii) is spin-1 PXP, with $P = |S_z = -1\rangle\langle S_z = -1|$, (iv) spin-1 PXP, with $P = |S_z = 0\rangle\langle S_z = 0|$, (v) spin-1 PXP, with $P = |S_z = 1\rangle\langle S_z = 1|$, (vi) $N_c = 3$ -color clock model, (vii) free paramagnet. From this we conclude that for the on-site Hilbert space dimension $N_c = 3$, the only scarred models are obtained by various ways one can constrain a free paramagnet. As mentioned in the main text, the maximum fidelity of the clock model 0.7237 is greater than the spin-1 model, 0.6534. This improvement in the revival fidelity is seen in all N_c -odd models. For example, at $N_c = 5$, $N = 10$, spin: 0.5626, clock: 0.7656. Thus, by constraining the free paramagnet with P' as opposed to P^0 leads to better revivals for N_c odd. Finally, although still expressible as spin models, the clock basis provides a much simpler interpretation of the dynamics, clearly showing a period of free precession followed by an interacting segment.

In Fig. S3 we compare the 5-color clock with the PXP spin-2 model and the 6-color clock with the PXP spin 5/2 model. The different choice of the projector (P^0 or P') leads to a rather different structure of the scar states near the edge of the spectrum. While the corresponding clock and spin models both contain the same number of scar states, we see the band of scars remains better separated from the bulk near the edge of the spectrum in the clock models. Fidelity decays similarly in both models, but the spin model lacks the period of free precession observed in clock models in the main text, instead just bouncing back and forth between Néel and anti-Néel states, $|0404\dots\rangle$ and

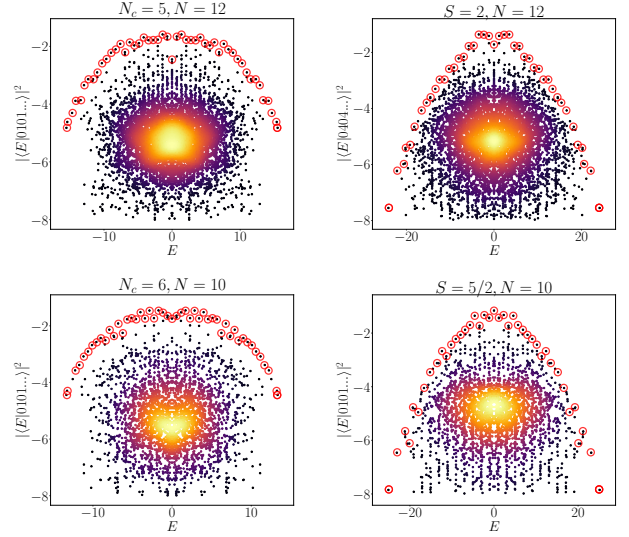


Figure S3. Comparison of the scarred band of states for 5-color clock model and PXP spin-2 model. Each plot shows overlap of all eigenstates with the product state $|0404\dots\rangle$. While the total number of scarred states is the same in the two models, the shape of the scarred band is quite different.

$|4040\dots\rangle$, as in spin-1/2 PXP. Clock models were found to “shed” less fidelity for odd N_c , where the difference in the first revival peak maximum of $|\langle\psi(t)|\psi(0)\rangle|^2$ was found to be 0.2261 for $N_c = 5$. For even N_c , however, the maximum fidelity is comparable between clock and spin models.

RELATION TO CHIRAL CLOCK MODELS

By analogy with the quantum Ising model in a transverse field, Fendley has studied generalizations of models that involve clock operators [41], originally introduced by Baxter [51]. Instead of focusing on critical properties of such models, we mainly focus on their fixed point, where only the shift operator is present in the Hamiltonian. The first non-trivial case that is distinct from our clock operators occurs for $N_c = 4$ Chiral Clock Model (CCM) [41], with the Hamiltonian defined as:

$$H = f \sum_{j=1}^N \tau_j^\dagger e^{-i\phi} + J \sum_{j=1}^{N-1} \sigma_j^\dagger \sigma_{j+1} e^{-i\theta} + h.c., \quad (\text{S4})$$

where the operators σ and τ generalize the spin-1/2 Pauli matrices, σ_z and σ_x , respectively. They are given by

$$\sigma_j = \begin{pmatrix} 1 & 0 & 0 & 0 \\ 0 & \omega & 0 & 0 \\ 0 & 0 & \omega^2 & 0 \\ 0 & 0 & 0 & \omega^3 \end{pmatrix}, \quad \tau_j = \begin{pmatrix} 0 & 1 & 0 & 0 \\ 0 & 0 & 1 & 0 \\ 0 & 0 & 0 & 1 \\ 1 & 0 & 0 & 0 \end{pmatrix}, \quad (\text{S5})$$

where (for $N_c = 4$) we have $\omega = i$. Taking $J = 0$, $\phi = -\pi/2$, the Hamiltonian (S4) becomes non-interacting,

with the on-site Hamiltonian reducing to:

$$H^{site} = \begin{pmatrix} 0 & -i & 0 & i \\ i & 0 & -i & 0 \\ 0 & i & 0 & -i \\ -i & 0 & i & 0 \end{pmatrix}. \quad (S6)$$

We construct an interacting many-clock model by introducing the same Rydberg-like constraint:

$$H_{chiral} = \sum_j P_{j-1} H_j^{site} P_{j+1}, \quad (S7)$$

with $P_j = |0_j\rangle\langle 0_j|$. This Hamiltonian can be obtained as the deformation of our clock model introduced in the main text.

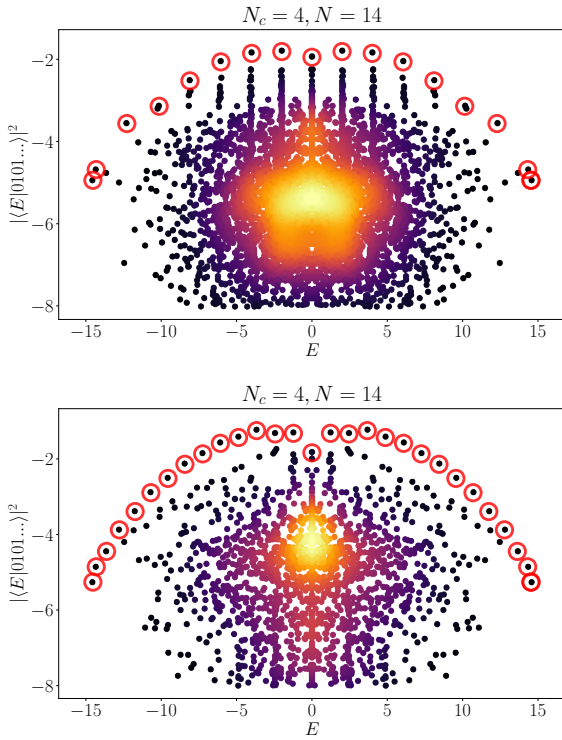


Figure S4. Overlap of all eigenstates of CCM, Eq. (S7), with product state $|0101\dots\rangle$ (top) and $|0202\dots\rangle$ (bottom). System size $N = 14$. $|0101\dots\rangle$ has $N+1$ scars, while $|0202\dots\rangle$ has $N+2$ scars.

In Fig. S4 we plot the overlap of all eigenstates of the Hamiltonian in Eq. (S7) with two product states: $|1010\dots\rangle$ (top) and $|2020\dots\rangle$ (bottom). System size is for $N = 14$ with periodic boundary conditions. These plots show that the model is not completely ergodic and supports a band of scarred states. However, the scarred bands look rather different in the two cases, with a stronger clustering of eigenstates into towers for the case of $|1010\dots\rangle$ state. We note that the structure of the scarred band in the bottom panel of Fig. S4 is quite reminiscent of the PXP spin-1/2 model [28]. In fact, as

we show next, the dynamics in this case reduces to the same type of oscillation that was found in the PXP spin-1/2 model.

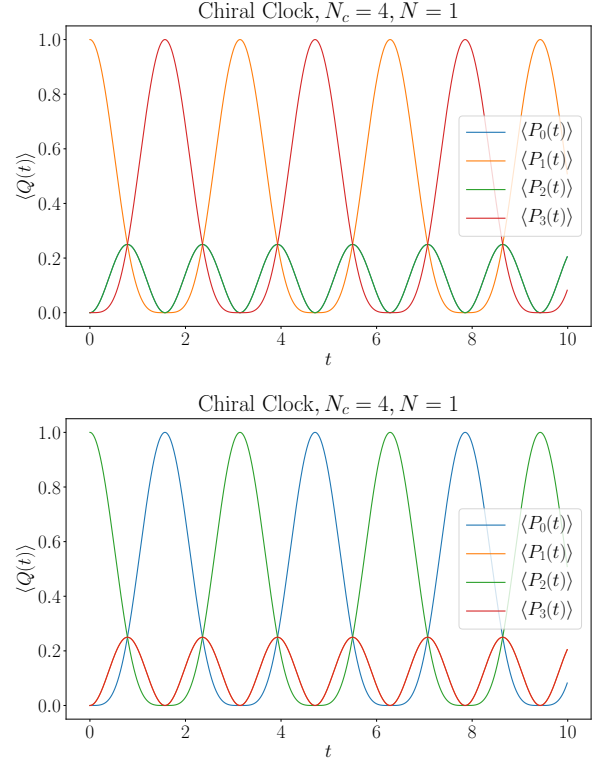


Figure S5. Single site precession of the unconstrained H_{site} model in Eq. (S6). The dominant dynamics is $0 \rightarrow 2$ flips and $1 \rightarrow 3$ flips.

Fig. S5 shows the single site precession of H^{site} in the absence of a constraint. We see that the dominant dynamics is $0 \rightarrow 2$ flips and $1 \rightarrow 3$ flips. Thus, when the constrained model, dressed with P^0 , is quenched from $|0101\dots\rangle$, the dominant dynamics is just to oscillate between $|0101\dots\rangle \rightarrow |0303\dots\rangle$, as $0 \rightarrow 2$ is blocked due to the constraint. Neglecting leakage, this is just a decoupled free paramagnet precessing at every other site. However, when quenched from $|0202\dots\rangle$, a transition through the polarized state $|0000\dots\rangle$ is permitted and we see transitions like $|0202\dots\rangle \rightarrow |2020\dots\rangle$, reminiscent of spin-1/2 PXP.

We confirm this by studying the fidelity time series, shown in Fig. S6, for two initial states, $|\psi_0\rangle = |1010\dots\rangle$ (top) and $|\psi_0\rangle = |2020\dots\rangle$. As in the main text, to get a clearer insight into the dynamics, we plot the generalized fidelity, $|\langle\phi|\exp(-itH)|\psi_0\rangle|^2$, where for $|\phi\rangle$ we do not necessarily pick the initial state, but any $|n0n0\dots\rangle$, $n = 1, 2, 3$, and their translated copies, $|0n0n\dots\rangle$. We notice that the predominant dynamics of this Hamiltonian is to drive oscillations between the $|1\rangle$, $|3\rangle$ states and the $|0\rangle$, $|2\rangle$ states, with a small leakage into the remaining states. When quenched from $|0101\dots\rangle$, as $0 \rightarrow 2$ is

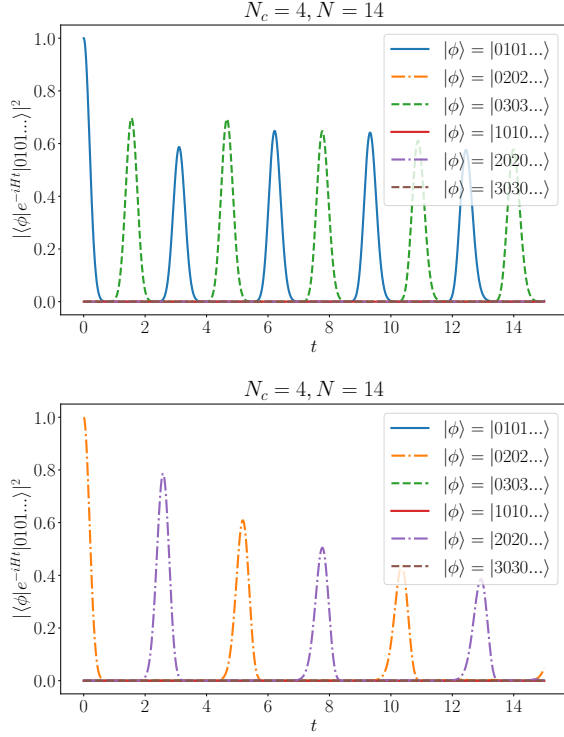


Figure S6. Fidelity of revivals in CCM, Eq. (S4), from the initial states $|1010\dots\rangle$ (top) and $|2020\dots\rangle$ (bottom). System size $N = 14$. The plots show $|\langle\phi|\exp(-itH)|\psi_0\rangle|^2$, where for $|\phi\rangle$ is any of $|n0n0\dots\rangle$, $n = 1, 2, 3$, and their translated copies, $|0n0n\dots\rangle$.

blocked due to the Rydberg constraint, the resulting dynamics is primarily just a free precession of the decoupled spin-1/2 chain, with a small leakage. This is observed in Fig. S6, where we see transitions between $|0101\dots\rangle \rightarrow |0303\dots\rangle$ without passing through $|0000\dots\rangle$. In contrast, $0 \rightarrow 2$ flips are permitted when quenching from the state $|2020\dots\rangle$. This allows the state to evolve through the polarized state $|0000\dots\rangle$ and exchange sublattices, undergoing oscillations between $|0202\dots\rangle \rightarrow |2020\dots\rangle$. This is precisely the same dynamics of spin-1/2 PXP, neglecting the leakage. As we see in Fig. S6 (bottom), we obtain non-zero fidelity only with the states $|2020\dots\rangle$ and $|0202\dots\rangle$, suggesting that the 4-color chiral clock model contains an embedded PXP spin-1/2.

Finally, we note that CCMs, as defined in Ref. [41], appear to have scars only in $N_c \leq 4$ cases. For odd $N_c \geq 5$, we did not find revivals from Néel-type initial states. However, we note that for N_c -even it is possible to construct a special case of our clock models by choosing $k_n \in \{-N_c/2, \dots, -1, 1, \dots, N_c/2\}$. These models *do* appear to support scars, and for $N_c = 4$ this choice of k 's reduces to CCM in Eq. (S4). Nevertheless, for $N_c > 4$ longer range couplings are introduced and the models are no longer equivalent to Ref. [41]. The scarring in these models can similarly be explained by studying the

single-site free precession, where dominant cyclic transitions between basis states emerge, with cycles shorter than N_c . Ignoring leakage away from these paths, they are effectively the same as the corresponding clock model with a matching cycle length.

ANALYTIC PREDICTION OF PARAMETERS OF 4-COLOR SCARRED MODELS

In the main text we presented a phase diagram of $N_c = 4$ models of the form $H = \sum_n P_{n-1}^0 C_n P_{n+1}^0$, which were shown to contain strong revivals. We noted that optimal models in these diagrams could be roughly predicted by determining the values of parameters that yield a single-site Hamiltonian C with evenly spaced eigenvalues, such that the single-site dynamics is periodic. Further models with weaker revivals are obtained for C whose eigenvalue spacings differed by a ratio of 2. In the following we derive analytical expressions for the lines in Fig. 2 in the main text.

Varying the matrix elements of C , we consider all Hermitian, purely imaginary, non-diagonal C , in analogy with the clock and spin Hamiltonians discussed in the main text. We are free to rescale C such that one coupling has magnitude 1, so for $N_c = 4$, 5 couplings can be varied. We consider two slices of the phase diagram: (A) vary the next-nearest neighbor hoppings, $C_{02} = C_{13} = \alpha i$, while also varying $C_{03} = -\beta i$; (B) switch off next-nearest-neighbor hoppings while varying $C_{12} = -\alpha i$ and $C_{03} = -\beta i$. Explicitly:

$$C_n^{(A)} = \begin{pmatrix} 0 & -i & \alpha i & -\beta i \\ i & 0 & -i & \alpha i \\ -\alpha i & i & 0 & -i \\ \beta i & -\alpha i & i & 0 \end{pmatrix}, \quad (\text{S8})$$

$$C_n^{(B)} = \begin{pmatrix} 0 & -i & 0 & -\beta i \\ i & 0 & -\alpha i & 0 \\ 0 & \alpha i & 0 & -i \\ \beta i & 0 & i & 0 \end{pmatrix}. \quad (\text{S9})$$

The characteristic eigenvalue equation for both these matrices reduces to the form

$$E^4 - aE^2 + b = 0, \quad (\text{S10})$$

with a and b being:

$$\text{(A)} \quad a = 3 + 2\alpha^2 + \beta, \quad (\text{S11})$$

$$b = 2\beta - 2\alpha^2 - 2\alpha^2\beta + \alpha^4 + \beta^2 + 1, \quad (\text{S12})$$

$$\text{(B)} \quad a = \alpha^2 + \beta^2 + 2, \quad (\text{S13})$$

$$b = 2\alpha\beta + \alpha^2\beta^2 + 1. \quad (\text{S14})$$

It follows that the eigenvalues E take the form

$$E_{1,\dots,4} = \mp \frac{1}{\sqrt{2}} \sqrt{a \pm \sqrt{a^2 - 4b}}.$$

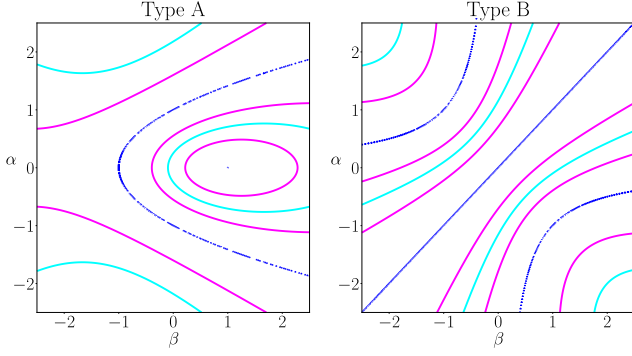


Figure S7. Prediction of scarred models with strongest revivals based on the eigenvalue spacings of C for $N_c = 4$. Left and right panels refer to two deformations of C in Eqs. S8, S9. Plotted here are: (a) equidistant eigenvalues, Eq. (S15) (cyan), (b) eigenvalue spacings commensurate with ratio 2 (pink), Eq. (S16), (S17), (c) degenerate eigenvalues, Eq. (S18), (S19) (blue). These lines coincide with the regions of strong revivals in Fig. 2 in the main text.

These eigenvalues are symmetric about zero, such that the spacings $\Delta E_1 = \Delta E_3$, with $\Delta E_n = E_n - E_{n-1}$. The analytic prediction for robust scarred models, based on the single-site analysis, then reads:

- Equidistant eigenvalues:

$$9a^2 = 100b, \quad \Delta E_2 = \Delta E_1, \quad (\text{S15})$$

- Commensurate eigenvalues with ratio 2:

$$4a^2 = 25b, \quad \Delta E_2 = 2\Delta E_1, \quad (\text{S16})$$

$$25^2 = 676b, \quad \Delta E_2 = \frac{1}{2}\Delta E_1, \quad (\text{S17})$$

- Degenerate eigenvalues:

$$a^2 = 4b, \quad \Delta E_1 = \Delta E_3 = 0, \quad (\text{S18})$$

$$b = 0, \quad \Delta E_2 = 0 \quad (\text{S19})$$

These equations are plotted in terms of parameters α, β in Fig S7. These lines give the band of scarred models in our $N_c = 4$ phase diagram in Fig. 2 in the main text.

APPROXIMATING SCARRED EIGENSTATES

In the PXP spin-1/2 model [20, 28] an approximation scheme called “the forward scattering approximation” (FSA) was introduced in order to approximate the $N + 1$ scarred eigenstates in a chain of size N . This approximation was shown to accurately capture the eigenstates that have highest overlaps with the Néel state and whose energies are equally spaced. The FSA is formally

based on the splitting of the Hamiltonian into two parts, $H = H^+ + H^-$, where H^+ increases the Hamming distance from the Néel state by one (and H^- , conversely, decreases this distance by one). The FSA is defined by projecting the PXP Hamiltonian into the $(N + 1)$ -dimensional basis spanned by vectors $(H^+)^n |1010\dots\rangle$, $n = 0, 1, \dots, N$. By construction, these vectors are orthogonal to each other. Diagonalizing the PXP Hamiltonian in this basis produces approximate eigenenergies and eigenvectors, which were found to match the exact ones with high accuracy. Moreover, the projection of the Hamiltonian into the FSA basis can be performed analytically, allowing one to reach much larger sizes than in exact diagonalization. Finally, the FSA scheme also provided an intuitive picture for the quench dynamics in terms of the wave function spreading over the Hilbert space graph [20].

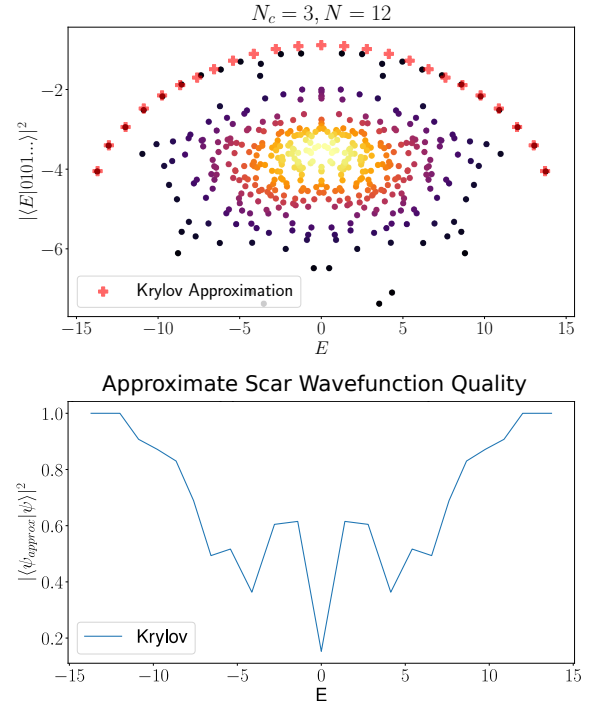


Figure S8. Quality of scar approximations obtained by projecting H into the $2N + 1$ Krylov subspace, using $|0101\dots$ as the initial vector.

Unfortunately, direct generalization of the FSA to $N_c > 2$ clock models is not trivial. In retrospective, in the PXP case, the splitting of the Hamiltonian into H^+ and H^- is straightforward because we can rely on the conventional definition of the Hamming distance. In the higher color models, this is no longer sufficient; moreover, it may be necessary to split the Hamiltonian into more than two parts. Nevertheless, in Fig. S8 we demonstrate that a more general approximation scheme yields accurate results for the $N_c = 3$ clock model. Instead of splitting H , we follow the standard Lanczos

procedure and build the Krylov subspace using full H : $\mathcal{K} = \{H^n|1010\dots\rangle, n = 0, 1, 2, \dots\}$. Compared to the FSA, the Krylov subspace may contain an arbitrary number of vectors and we need to explicitly impose a cutoff. Furthermore, the Krylov vectors are no longer necessarily orthogonal, and Gram-Schmidt orthogonalization needs to be explicitly performed. We note that this approximation scheme is identical to the standard Lanczos algorithm for approximating the *ground state* of a system. In that case, however, the size of the Krylov subspace can be as large as as required to reach a target precision, while in our case we stop the algorithm after a given number of steps. Moreover, we obtain approximations to *all* scarred states in a single run of the algorithm.

Fig. S8(top) shows the result of the Krylov approximation for the 3-color clock model. We see that the approx-

imation accurately predicts the energies of scarred eigenstates, as well as the eigenstate overlap with $|1010\dots\rangle$ product state. Fig. S8(bottom) also shows the overlap of the predicted scarred wave functions with those obtained by exact diagonalization. The approximation is very accurate for the ground state, which is expected given that we are effectively using the Lanczos algorithm. Neglecting the zero energy state (which is not uniquely defined due to large degeneracy at $E = 0$), the average overlap with the exact states for $N_c = 3, N = 12$ is 0.7410. This is considerably smaller compared to PXP 1/2, where the same procedure results in an average accuracy of 0.9173. Moreover, the explicit orthogonalization that needs to be performed numerically restricts the Krylov approximation scheme to much smaller system size compared to the FSA.